Phantom Validation of DCE-MRI Magnitude and Phase-Based Vascular Input Function Measurements

Warren Foltz[1,2], Brandon Driscoll[1], Sangjune Laurence Lee[2], Krishna Nayak[3], Naren Nallapareddy[3], Ali Fatemi[2], Cynthia Ménard[4,6], Catherine Coolens[1,2,4,6], and Caroline Chung[5,7]

[1]Department of Medical Physics, Princess Margaret Cancer Center and University Health Network, Toronto, ON, Canada; [2]Department of Radiation Oncology, University of Toronto, Toronto, ON, Canada; [3]Ming Hsieh Department of Electrical Engineering, Viterbi School of Engineering, University of Southern California, Los Angeles, CA; [4]Department of Radiation Oncology, Centre Hospitalier Universite de Montreal, Montreal, Canada; [5]TECHNA Institute, University Health Network, Toronto, ON, Canada; [6]Department of Biomaterials and Biomedical Engineering, University of Toronto, Toronto, ON, Canada; and [7]Department of Radiation Oncology, MD Anderson Cancer Center, Houston, TX

Corresponding Author:
Catherine Coolens, PhD
Princess Margaret Cancer Centre, Radiation Medicine Program,
Rm 6:306 - 700 University Avenue, Toronto, ON M5G 1Z5, Canada;
E-mail: catherine.coolens@rmp.uhn.ca.

Key Words: dynamic contrast-enhanced MRI (DCE-MRI), permeability, arterial input function (AIF), quantification, MRI phase, phantom

Abbreviations: Arterial input functions (AIF), magnetic resonance imaging (MRI), computed tomography (CT), dynamic contrast-enhanced magnetic resonance imaging (DCE-MRI), field of view (FOV), magnetic resonance (MR), echo time (TE), repetition time (TR), regions of interest (ROIs), signal-to-noise ratio (SNR)

ABSTRACT

Accurate, patient-specific measurement of arterial input functions (AIF) may improve model-based analysis of vascular permeability. This study investigated factors affecting AIF measurements from magnetic resonance imaging (MRI) magnitude (AIF_{MAGN}) and phase (AIF_{PHA}) signals, and compared them against computed tomography (CT) (AIF_{CT}), under controlled conditions relevant to clinical protocols using a multimodality flow phantom. The flow phantom was applied at flip angles of 20° and 30°, flow rates (3–7.5 mL/s), and peak bolus concentrations (0.5–10 mM), for in-plane and through-plane flow. Spatial 3D-FLASH signal and variable flip angle T1 profiles were measured to investigate in-flow and radiofrequency-related biases, and magnitude- and phase-derived Gd-DTPA concentrations were compared. MRI AIF performance was tested against AIF_{CT} via Pearson correlation analysis. AIF_{MAGN} was sensitive to imaging orientation, spatial location, flip angle, and flow rate, and it grossly underestimated AIF_{CT} peak concentrations. Conversion to Gd-DTPA concentration using T1 taken at the same orientation and flow rate as the dynamic contrast-enhanced acquisition improved AIF_{MAGN} accuracy; yet, AIF_{MAGN} metrics remained variable and significantly reduced from AIF_{CT} at concentrations above 2.5 mM. AIF_{PHA} performed equivalently within 1 mM to AIF_{CT} across all tested conditions. AIF_{PHA}, but not AIF_{MAGN}, reported equivalent measurements to AIF_{CT} across the range of tested conditions. AIF_{PHA} showed superior robustness.

INTRODUCTION

Dynamic contrast-enhanced magnetic resonance imaging (DCE-MRI) is a useful tool to measure blood vessel permeability and volume fractions within heterogeneous lesions, such as tumors (1). There is growing interest in the role of early changes in tumor vascularity as predictive biomarkers of tumor response to therapy, particularly with increasing use of antiangiogenic agents, recognizing that changes in tumor physiology can often precede tumor volume changes (1-3). Biomarkers of early response to treatment introduce the potential to individualize cancer treatment based on individual responses, but the current challenge is determining the optimal approach for acquiring and interpreting these biomarker measures. To date there has been wide variability in the reported DCE-MRI findings and responses across different institutions and this may, at least in part, reflect the variability in image acquisition and analysis (4, 5).

Analysis of DCE-MRI data commonly assumes a 2-compartmental model to generate functional parameters, such as the permeability surface area product per unit volume (K^{trans}), size of the extracellular extravascular space (v_e), and efflux rate constant (k_{ep}) (6, 7). Accurate quantification of these permeability kinetic parameters is dependent on the application of an accurately measured arterial input function (AIF) from a major vessel in the vicinity of the tumor (8). Typically, the AIF has been evaluated by using the magnetization magnitude signal in an artery, but the conversion from magnitude signal to absolute gadolinium contrast agent concentration (eg, Gd-DTPA) is susceptible to a number of factors including blood inflow effects, radiofrequency transmit field (B_1) inhomogeneity, slice profile

ISSN 2379-1381 http://dx.doi.org/10.18383/j.tom.2019.00001

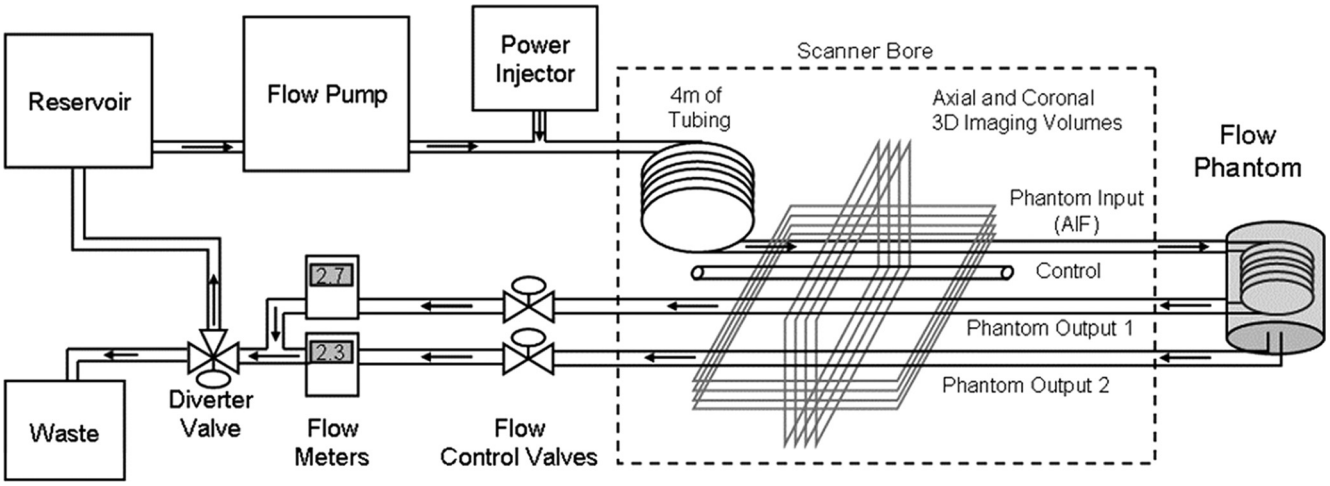

Figure 1. Simplified layout of the flow-phantom experiment. A high-concentration bolus is delivered from the pump and power injector through the phantom input tube into the flow phantom, where it divides into phantom output tubes 1 and 2, so that arterial input functions (AIFs) corresponding to each tube are captured within the same dynamic acquisition. The output flow ratios of the 2 phantom output tubes were set to 50:50 so that the velocity in each of the output tubes is half of that in the input tube. The diverter valve can channel the returning fluid to the reservoir for recirculation or to the waste for disposal (22).

effects, mis-registration susceptibility shifts, contrast agent dispersion, and hematocrit variation (9-12). Owing to these challenges, many studies have used the population-average AIF provided by vendor software for the generation of kinetic parameters from DCE-MRI data. Use of a population-average AIF may improve reproducibility in permeability kinetic parameters, but it may not result in accurate and meaningful quantification of kinetic parameters for individual patients (13, 14). Accurate measurement of an individual AIF may help improve both the accuracy and reproducibility of kinetic analysis (15, 16).

A growing body of work supports the use of the MRI signal phase for AIF measurement, for improved robustness relative to the magnitude signal (17-20). This study used an in-house-developed dynamic flow phantom (21) to investigate factors affecting the magnitude signal-derived AIF (AIF_{MAGN}), and to compare AIF_{MAGN} to the phase signal-derived AIF (AIF_{PHASE}) in a controlled environment with validation against the gold-standard computed tomography (CT)-derived AIF (AIF_{CT}). Both accuracy and robustness of the respective input functions were tested against varying imaging orientation, flip angles, flow rates, and peak AIF gadolinium contrast agent concentrations.

MATERIALS AND METHODS

Multimodal CT/MRI Flow Phantom

The basis of experimentation was an in-house-developed flow phantom (Figure 1), currently in use for accreditation of centers participating in multicenter clinical trials using DCE-CT in the province of Ontario (21). Physiological flow was simulated by a positive displacement pump (Compuflow 1000MR, Shelley Medical Imaging Technologies, London, ON), which pushed a blood-mimicking fluid consisting of a 15%–85% glycerol–water by volume mixture through the flow circuit. The 15%–85% glycerol–water mixture was pumped from an external reservoir through 1/4″ (6.35 mm) polyvinyl chloride tubing, and an in-line clinical power injector (Optistar Elite, Mallinckrodt, Cincinnati, OH) was used to simulate the contrast bolus representing the AIF (Phantom Input) by injecting various dilutions of Gadovist 1.0 (604 mg/ml, Bayer Corp., Leverkusen, DE). The flow phantom, based on a 2-compartmental exchange model, has 2 output tubes roughly representing the venous output function (phantom output 1) and the tissue signal function (phantom output 2). Fluid from the phantom outputs was fed back to the external reservoir for noncontrast experiments or to a waste container for contrast experiments.

Within flow rates up to 7.5 mL/s, the flow phantom provides high intrarun and intraday reproducibility with an error of $<2\%$ as validated through CT imaging.

The flow through the phantom output tubes is controlled by a set of flow control valves such that the output flow rates in each output tube is equal to half that of the input tube. The relationship between the phantom input peak concentration and that of the output tube peaks is variable, based on the choice of flow rate because exchange happens more quickly under higher rates of flow, but it is fully predictable based on the known geometry of the system.

Gold Standard CT_{AIF}

Gold standard CT_{AIF} measurements, shown in Figure 2, were acquired with a 320-slice scanner (Toshiba Medical Systems, Aquilion ONE) using a dynamic volume–time sequence operating at 120 kV, 300 mA gantry rotation of 0.5 seconds, and image frequency of 1 vol (160 mm longitudinal coverage) every 1.5

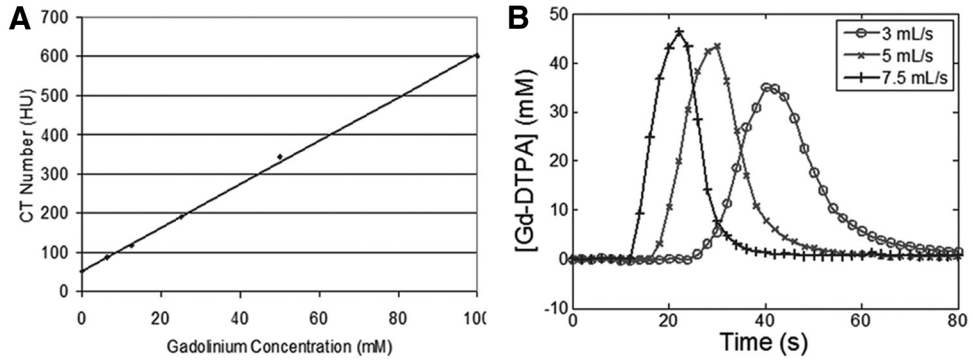

Figure 2. Gold standard AIF_{CT}: linearity of Hounsfield unit calibration with Gd-DTPA (A), Gold standard AIF_{CT} for 10 mM bolus injection at 3, 5, and 7.5 mL/s flow velocity (B).

seconds, with spatial resolution of 0.625 × 0.625 × 1 mm^3. The DCE-CT studies were performed at flow rates of 3, 5, and 7.5 mL/s, corresponding to average flow velocities of 9.5, 15.8, and 23.7 cm/s, at peak AIF Gd-DTPA concentration of 50 mM to improve CT signal-to-noise ratio (SNR). The peak CT-measured Gd-DTPA concentrations are linearly scaled to match those of corresponding MRI experiments, based on *a priori* validation of linearity between the CT Hounsfield Units and Gd-DTPA concentration (Figure 2).

MRI Methods

A consistent setup was used for both DCE-CT and DCE-MRI acquisitions. The in-flow and out-flow tubes were oriented parallel to B_0 to minimize susceptibility artifacts (22), and these tubes were placed above the spine array coil and below the 2-coil body array to allow for sensitive experimentation. A separate polyvinyl chloride tube filled with the 15%–85% glycerol–water mixture was placed within the imaging stack to provide a signal reference for MRI analysis. An additional 4 m of coil tubing was also wound within the MRI bore to allow for polarization of in-flowing spins.

All magnetic resonance (MR) imaging used a 3 T Verio System (IMRIS, Winnipeg, CA). Variable-flip-angle (VFA) T1 quantification and DCE experimentation used a 3-dimensional Fast Low Angle SHot (3D-FLASH) pulse sequences with shared geometric features (23). For axially oriented slice packages (eg, through-plane flow), 3D data sets were acquired over a 12.8- × 6.4- × 12-cm field of view (FOV) with 124 × 64 × 24 matrix, providing 1 × 1 × 5 mm voxels. For coronally oriented slice packages (eg, in-plane flow), the FOV was 19.2 × 9.6 × 7.2 cm, matrix size was 192 × 96 × 24, and voxels were 1 × 1 × 3 mm^3. All acquisitions used an echo time (TE) and repetition time (TR) of 1.86 milliseconds and 4.8 milliseconds, and a 500 Hz/pixel readout bandwidth. For dynamic scans, 3D-FLASH temporal resolution was 5 seconds with 36 repetitions including at least 3 repetitions at baseline flow before contrast agent injection to determine the average preinjection signal. The acquisition times were 37 seconds per flip angle for VFA-T1 (4 flip angles of 2°, 10°, 20°, 30°, 5 averages, iPAT factor 1), and 3 minutes 4 seconds for DCE-MRI (experiment-dependent flip angle, iPAT factor 2, 5-second temporal resolution, 38 repetitions).

Static Experiments

Gd-DTPA was diluted into 15%/85% glycerol/water and water-only at concentrations between 0 and 10 mM within 15-cc conical tubes. Within the 8-channel head coil of the 3 T Verio system, shimming was then performed using the 0 mM tube centrally placed, and surrounded by 6 control tubes containing water. 3D-FLASH acquisitions, including magnitude and phase reconstructions, were then performed. The central tube was then replaced with a tube of higher Gd-DTPA concentration and imaged without reshimming. This design reduced biases from coil sensitivity, and from shimming to an asymmetric distribution of samples with varying magnetic susceptiblity. It also provided a background phase correction, measured as the average phase drift across all 6 control tubes.

T1 relaxivity was measured using the body coil for RF transmit, and spine array coil elements and anteriorly placed small flexible coil for RF receive. T1 values were measured from all samples at once using an inversion recovery spin-echo technique (slice-selective inversion pulse; TE 12 milliseconds; TR 9350 milliseconds; inversion times 25, 50, 100, 200, 400, 800, 1200, 1600, 2000, 3500, 5000 milliseconds; FOV 240 × 192 mm; matrix 138 × 102; 5 mm slice thickness; iPAT factor 2; readout bandwidth 130 Hz/pixel; 10 minutes per inversion time). T1 relaxivity was extracted from the T1 and concentration data pairs via linear regression (OriginLab, Northampton, MA).

Dynamic Experiments

The complete set of dynamic experiments is summarized in Table 1. The input flow rate varied between 3, 5, and 7.5 mL/s (average flow velocities of 9.5, 15.8, and 23.7 cm/s), consistent with the physiologic range of internal carotid artery blood flow rates (24). For most runs, a peak concentration of 10 mM was delivered through the in-flow tube, which also provided assessment of peak concentrations of ~5 and 2.5 mM in the 2 outflow tubes. Lower peak AIF Gd-DTPA concentrations of ~0.5, 1, and 2 mM in the in-flow tube were also considered. This concentration range from 0.5 to 10 mM provided coverage of the full range of Gd-DTPA concentrations expected in a clinical DCE-MRI examination (25). Gd-DTPA concentration at peak enhancement was programmed by varying the dilution of Gd-DTPA within the power injector at constant injection volume of 16 mL and duration of 10 seconds.

Magnitude-Derived AIF: In-flow, RF, and Slice Profile Effects. Inhomogeneity of the RF transmit field and inflow affect the spatial profile and accuracy of the 3D-FLASH magnitude signal (23). Furthermore, inflow and RF transmit field inhomogeneity prolong the transition of the 3D-FLASH signal to steady-state

Table 1. List of AIF Experiments

Run #	Flow Rate (ml/s)	Peak Concentration (mM)	Imaging Plane	Flip Angle (Degrees)
1	7.5	10	Through-plane	20
2	7.5	10	Through-plane	20
3	5	10	Through-plane	20
4	5	10	Through-plane	20
5	5	10	Through-plane	20
6	5	10	Through-plane	20
7	3	10	Through-plane	20
8	3	10	Through-plane	20
9	5	5	Through-plane	20
10	5	5	Through-plane	20
11	5	2	Through-plane	20
12	5	2	Through-plane	20
13	5	1	Through-plane	20
14	5	1	Through-plane	20
15	5	0.5	Through-plane	20
16	5	0.5	Through-plane	20
17	7.5	10	Through-plane	30
18	5	10	Through-plane	30
19	3	10	Through-plane	30
20	5	5	Through-plane	30
21	5	2	Through-plane	30
22	5	1	Through-plane	30
23	5	0.5	Through-plane	20
24	7.5	10	In-plane	30
25	5	10	In-plane	20
26	7.5	10	In-plane	30

Imaging plane is stated as relative to the direction of flow; through-plane corresponds to an axial slice package; and in-plane corresponds to a coronal slice package. Flow rates of 3, 5, and 7.5 mL/s correspond to flow velocities of 9.5, 15.8, and 23.7 cm/s, respectively.

(9). Different RF inhomogeneity, slice profile, in-flow, and steady-state errors are to be expected for through-plane flow with an axial slice excitation and for in-plane flow with a sagittal or coronal slice excitation.

Spatial profiles of the 3D-FLASH signal were measured via acquisitions at flow rates from 0 to 23.7 cm/s and at flip angles from 2° to 30° for both axially and coronally oriented slice packages. Effects of flow rate and flip angle on the 3D-FLASH signal profile were confirmed via magnitude AIF measurements (through-plane and in-plane dynamic acquisitions at flip angles of 20° and 30° at flow rates of 5 mL/s and 7.5 mL/s and peak concentration of 10 mM. The magnitude AIF signals was scaled to Gd-DTPA concentration using T1 measured in a central slice using the variable flip angle technique.

Magnitude-Derived AIF: Correction Using VFA-T1. Endogenous T1 scales the conversion between the magnitude signal and Gd-DTPA concentration. However, in-flow accelerates the measured T1 relaxation based on the extent of spin displacement (26). Commonly used VFA-T1 measurements are very prone to bias from RF inhomogeneity, RF mistuning, and slice profile (23). Therefore, endogenous T1 values for blood taken from the literature or measured from static volumes may not be representative of true rates of repolarization at any location within the 3D-FLASH slice package in vivo. Geometrically equivalent 3D-FLASH VFA-T1 and DCE acquisitions at matched TR should be affected similarly by in-flow and RF errors. If so, MR signal to concentration conversion using position- and velocity-matched VFA-T1 instead of assumed T1 may improve the AIF_{MAGN} measurement.

The following acquisitions tested for improved AIF_{MAGN} using position- and velocity-matched VFA-T1. First, through-plane and in-plane 3D-FLASH image sets were measured at 2°, 10°, 20°, and 30° under static conditions. These image sets confirmed VFA-T1 at each location along the slice profile of the 3D-FLASH RF excitation pulse. Second, VFA-T1 maps were reconstructed from equivalent 3D-FLASH image sets acquired at flow rates of 3, 5, and 7.5 mL/s, to validate T1 acceleration with in-flow (26). Third, dynamic acquisitions at matching flow rates and flip angles of 20° and 30° were acquired during bolus Gd-DTPA injection with peak concentration of 10 mM and compared against DCE-CT to verify improved AIF accuracy when position- and velocity-matched VFA-T1 values were used rather than the VFA-T1 value at the center of the RF slice profile.

Phase-Derived AIF: Velocity and Concentration Effects. Compared to the magnitude-derived AIF, the phase-derived AIF should be insensitive to slice profile and in-flow effects. Phase-

and CT-derived AIFs for both axially and coronally oriented slice packages were compared at variable peak Gd-DTPA concentrations (0.5, 1, 2, 5, and 10 mM) and flow rates (9.5, 15.8, and 23.7 cm/s), across the entire slice profile.

Phase- and Magnitude-Derived AIFs: Comparison to CT. MRI AIF performance was tested against the CT gold standard via Bland–Altman difference and Pearson correlation analyses for all through-plane acquisitions in Table 1 (sample size of 69 given 23 runs, with readings from 1 phantom input and 2 phantom output tubes for each run). Further, 95% limits of agreement between the techniques for measurements in a single central slice were reported as the mean difference ± 1.96 standard deviance of the difference for the peak AIF concentration and the area under the curve (AUC) for the first 120 seconds after injection.

Phase- and Magnitude-Derived AIFs: Spatial Heterogeneity. Given the insensitivity to RF and in-flow effects, AIF_{PHA} should prove robust away from the central imaging slice. Spatial AIF_{MAGN} and AIF_{PHA} profiles were generated for 10 mM Gd-DTPA bolus injection at 23.7 cm/s flow velocity (5 mL/s). T1 measurements were matched to both velocity and slice position. Mean and standard deviations of T1-corrected AIF_{MAGN} and AIF_{PHA} were reported across the slice package for through-plane flow and across the field-of-view for in-plane flow.

Image Analysis

All MRI and CT signal and image data processing and analysis used Matlab® (MathWorks, Natick, MA). MR signal modeling used standard equations for magnitude and phase signal conversion to Gd-DTPA concentration, as follows:

$$S = S_0 \sin(\alpha)(1 - E_1)/(1 - E_1\cos(\alpha))e^{-TE/T2^*} \quad (1)$$

where $E_1 = \exp(-TR/T1)$, α is the flip angle, and S_0 and S are the relative signal enhancements before contrast injection and after contrast injection, respectively (27).

Magnitude signal enhancement was converted to concentration according to Schabel and Parker (28) with the following equation:

$$1/T_1(C) = 1/T_{10} + r_1 C \quad (2)$$

where T_{10} and T1 are the spin-lattice relaxation times before and after contrast injection, respectively; r_1 is the relaxivity of the contrast agent in the 15%–85% glycerol–water mixture; and C is the concentration of the Gd-DTPA contrast agent (27). For dynamic image analysis, the average of signals at the first 3 time points provided an estimate of the signal baseline.

The change in signal phase was converted to Gd-DTPA concentration with the following equation:

$$\Delta\varphi = TE\,\pi\gamma B_0 \chi_m \Delta C(\cos^2\theta - 1/3) \quad (3)$$

where γ is the proton gyromagnetic ratio (4.258×10^7 Hz/T), B_0 is the magnitude of the main magnetic field in Tesla, χ_m is the molar susceptibility of the Gd-DTPA concentration (3.4×10^7 mM^{-1} for Gd, in MKS units), and θ is the angle of the vessel relative to the main magnetic field ($\theta = 0$ being parallel with that field) (19). Concentration profiles of AIF_{PHA} were compensated for background phase drifts by subtraction of the phase signal within the 15%–85% glycerol–water control tube (18). The background phase drifts between baseline and final dynamic frames corresponded to Gd-DTPA concentration changes of 0.6 ± 0.2 mM, averaged across all 23 through-plane acquisitions and 2 control tubes.

Mean and standard deviations of signals were extracted from regions of interest (ROIs) for each of the 3 flow tubes. Analysis of axially oriented images used circular ROIs drawn on the AIF and control tubes in each of the 24 axial reconstructed slices. Coronal image analysis used 12 ROIs drawn equally spaced along the z-direction with both AIF and control tubes on a single coronal section that bisected each tube. Phase images were manually unwrapped if the ROI contained a phase 360° to 0° discontinuity by shifting modulo 360° until the discontinuity disappeared.

Statistical Analysis

Pearson correlations and linear regressions of peak Gd-DTPA concentrations and AUC measurements between CT and different MR data sets (magnitude, magnitude T1-corrected, and phase) were performed in MATLAB (The MathWorks) for both peak and AUC.

RESULTS

Static Experiments

Using the inversion recovery technique, an endogenous VFA-T1 of 1935 ± 40 milliseconds and T1 relaxivity of 7.5 ± 0.1 1/mM* milliseconds (R = 0.9998) were measured (Figure 3, A and B). The corresponding values for the Gd-DPTA–water solutions were 3007 ± 76 milliseconds and 5.0 ± 0.1 1/mM* milliseconds. Gd-DTPA concentrations derived from the magnitude signal were badly truncated to 2.5 mM using a 10° flip angle, but the Gd-DTPA concentration to 5 mM using a 20° flip angle, and to 10 mM using a 30° flip angle (Figure 3C). Linear and accurate measurement of Gd-DTPA concentration from the phase signal was observed after background phase correction (Figure 3D).

Dynamic Experiments

Magnitude-Derived AIF: In-flow, RF, and Slice Profile Effects. Spatial 3D-FLASH signal profiles are presented in Figure 4. In this figure, a completed transition to steady state was visualized as an equalization of signal magnitude with the static (0 cm/s) case. Flow data acquired with a 2° flip angle did not deviate much from the static experiment. At a 10° flip angle, considerable inflow bias was observed across the entire slice package at flow velocities above 3.2 cm/s for through-plane flow data (Figure 4C), whereas in-plane flow data were effectively acquired in steady-state at 0.6 relative to the FOV for flow velocities up to 30 cm/s (9.5 mL/s) (Figure 4D). With increasing flip angle above 10°, the extent of in-flow bias was reduced. Correspondingly, Figure 5 confirms improved, yet underestimated, magnitude-derived AIF estimation using higher flip angle acquisitions (20° and 30° for through-plane flow; 20° for in-plane flow at flow rates of 5 and 7.5 mL/s).

Magnitude-Derived AIF: Correction Using VFA-T1. Figure 6 confirms that in-flow and RF-related biases on the 3D-FLASH magnitude signal are encoded in VFA-T1 for through-plane measurements. Under no-flow conditions, axial VFA-T1 was uniform within 10% across 40% of the 12-cm slice package, and reduced sharply towards zero outside of the plateau region of the RF pulse profile. In comparison, coronal VFA-T1 was uniform

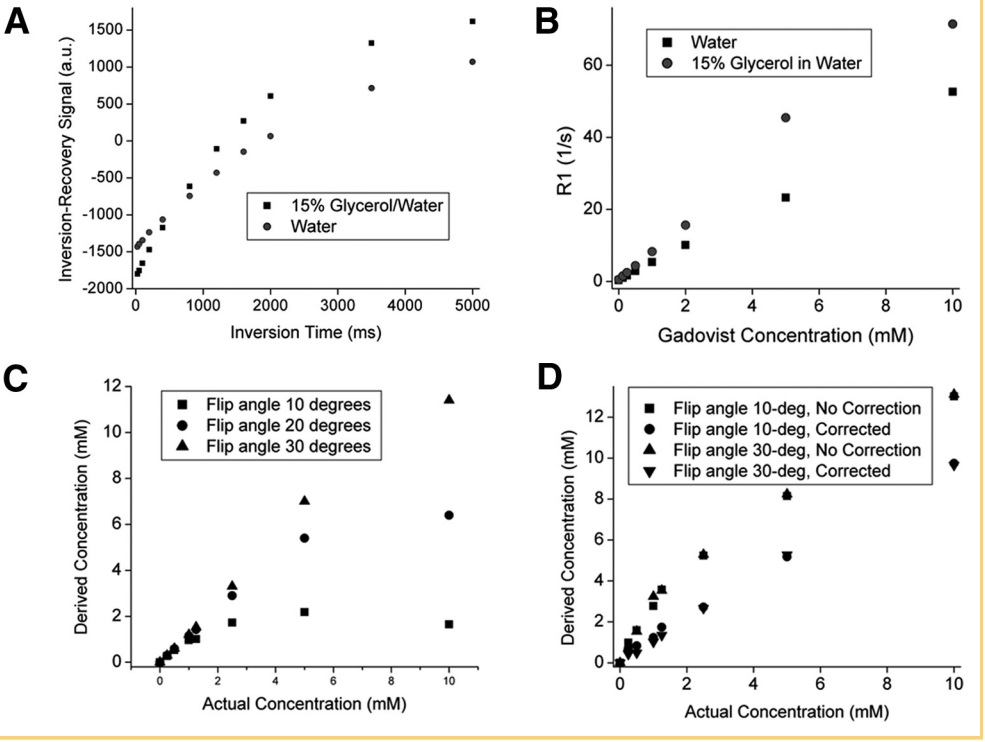

Figure 3. Static experiment results: Inversion-recovery signal as a function of inversion time for pure water and the 15% glycerol/water mixture (A). T1 and concentration data pairs used for T1 relaxivity calculations (B). Magnitude-derived concentration estimates against truth for flip angles of 10°, 20°, and 30° (C). Phase-derived concentration estimates against truth for flip angles of 10° and 30°, with and without background phase correction (D).

within 10% over 60% of the 19.2-cm FOV, and then reduced gradually, reflecting the RF inhomogeneity of the body transmit coil. Through-plane flow shifted the VFA-T1 profile in the direction of flow at increasing velocities, yet in-plane flow introduced only minor deviations to the VFA-T1 profile. Figure 7 confirms considerable improved, yet underestimated, AIF_{MAGN} accuracy compared to AIF_{CT} by using velocity-matched VFA-T1 measurements for signal-to-concentration conversion.

Phase-Derived AIF: Velocity and Concentration Effects. Figure 8A compares AIF_{PHA} and AIF_{CT} within a central slice across varying Gd-DTPA concentrations (0.5 to 10 mM) for through-plane flow at a fixed input flow rate of 5 mL/s. After

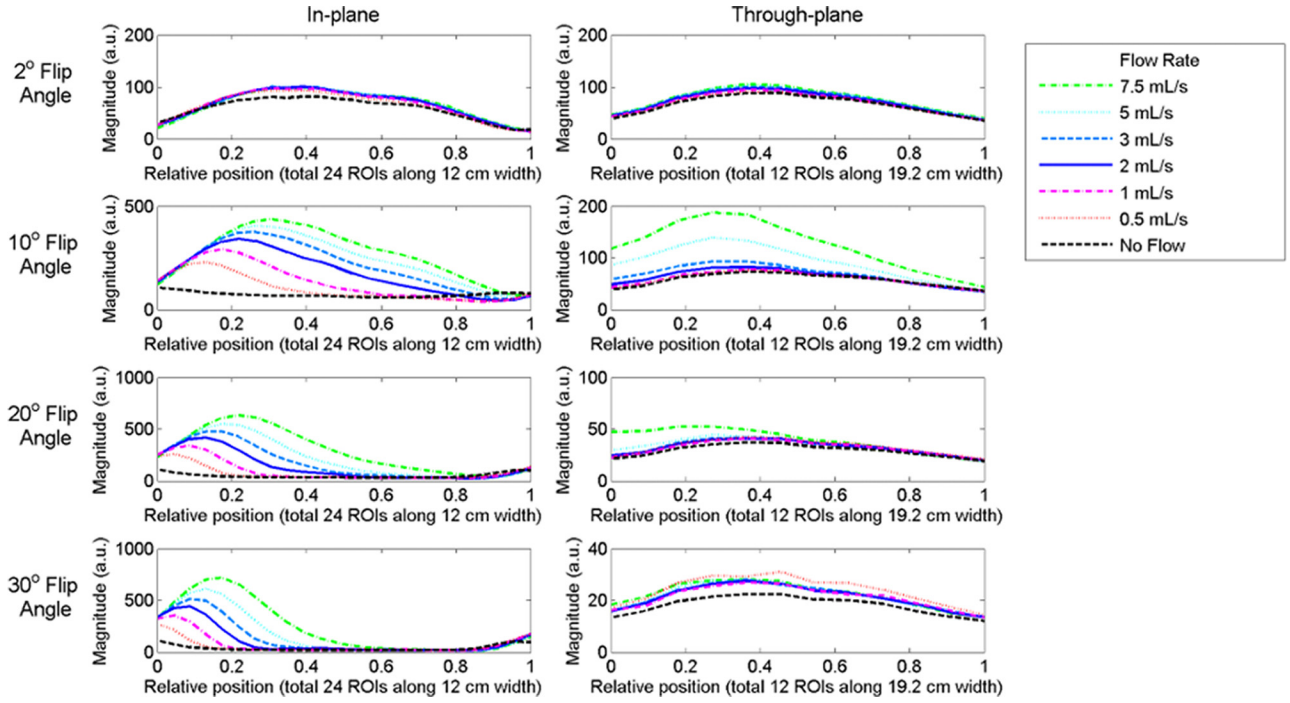

Figure 4. 3D FLASH signal profiles at varying flip angles and flow rates, corresponding to the range of velocities in the phantom input and 2 output tubes without Gd-DTPA for through-plane and in-plane orientations.

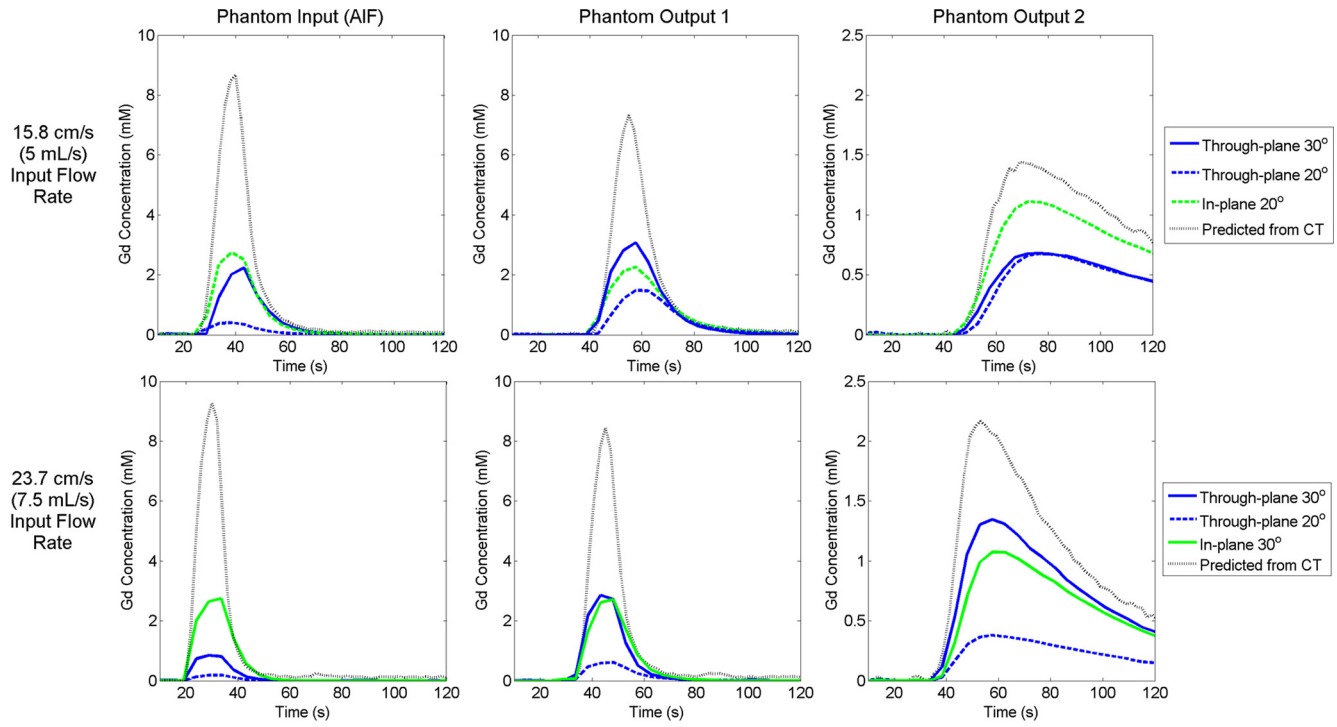

Figure 5. Magnitude and computed tomography (CT)-derived AIFs acquired at 10 mM peak Gd-DTPA concentration acquired for in-plane and through-plane flow orientations at multiple flip angles and 2 flow velocities.

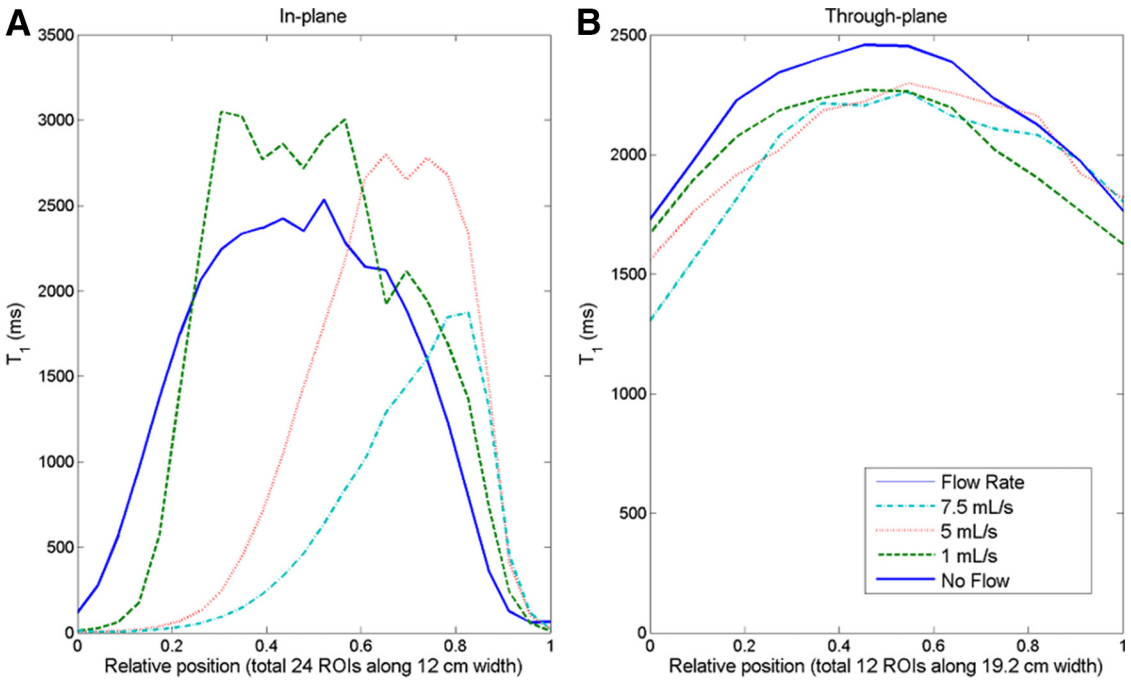

Figure 6. VFA-T1 measured at flow rates ranging from 0 to 7.5 mL/s. VFA-T1 accelerated by through-plane flow across the 12-cm slice profile in the axial orientation (A). VFA-T1 accelerated by in-plane flow across the 19.2 cm field of view (FOV) at zero flow in the coronal orientation (B).

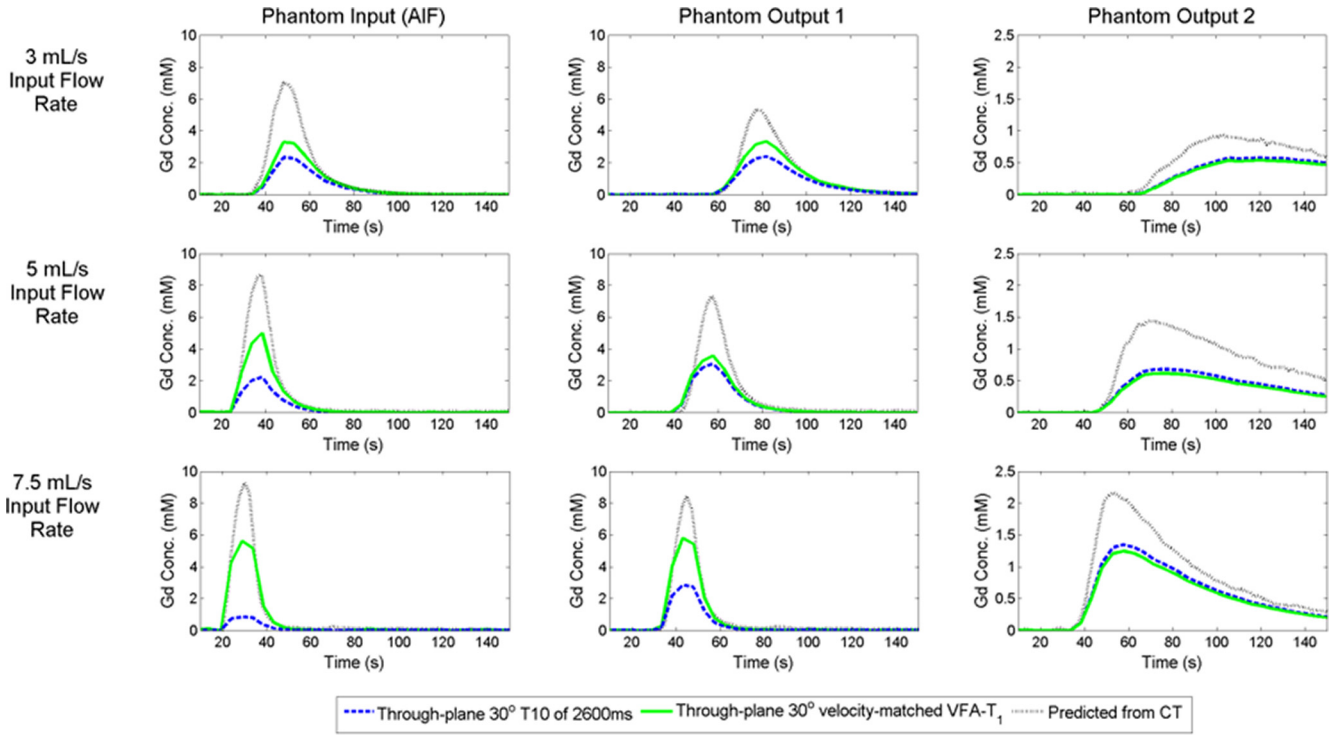

Figure 7. Accuracy in calculation of AIF_{MAGN} is improved using velocity-matched VFA-T1 at higher flow rates and Gd-DTPA concentrations. AIF_{MAGN} is compared to AIF_{CT} in a central slice at set peak concentration of 10 mM for through-plane flow at flow rates of (upper) 3, (middle) 5, and (lower) 7.5 mL/s for all 3 flow tubes (left—phantom input, middle—phantom output 1, right—phantom output 2).

background phase correction, the phase measurement tracked AIF_{CT} at Gd-DTPA concentrations above 1.6 mM, corresponding to phantom input and phantom output 1 tubes for input peak bolus >2 mM; yet, deviations were apparent in all phantom output 2 measurements and in all 1 mM peak bolus experiments. Figure 8B compares the same AIFs across varying input flow rates (3–7.5 mL/s) at a fixed input concentration of 10 mM. Under these conditions, AIF_{PHA} again tracked AIF_{CT} accurately.

Phase- and Magnitude-Derived AIFs: Comparison to CT. Pearson correlation analysis presented in Figure 9 reported the following trends: (A) bias in AIF_{MAGN} increased with Gd-DTPA concentration and reduced with flip angle; (B) T1 correction improved the AIF_{MAGN} measurement, but the 95% limits of agreement were prohibitively broad; and (C) phase-corrected AIF_{PHA} tracked AIF_{CT}. Difference analysis, summarized in Table 2, reported equivalence of AIF_{PHA} with AIF_{CT} within 1 mM for both peak concentration and within 20 mM*s AUC across all tested conditions, and that AIF_{MAGN} measurements approached equivalence with AIF_{CT} only at concentrations below 2 mM.

Phase- and Magnitude-Derived AIFs: Spatial Heterogeneity. For the through-plane flow, AIF_{PHA} reported mean and standard deviation values of 9.6 ± 0.5 mM for peak concentration and 28 ± 7 mM*s for AUC, across the middle 60% package of slices. For in-plane flow, AIF_{PHA} reported mean and standard deviation values of 9.2 ± 1 mM for peak concentration and 27 ± 14 mM*s for AUC, across the central 60% of the FOV. In comparison, T1-corrected AIF_{MAGN} using flip angles of 20° and 30° reported 4.0 ± 0.3 mM (through-plane) and 7 ± 2 mM (in-plane) for peak concentration, and 13 ± 1 mM*s (through-plane) and 20 ± 4 mM*s (in-plane) for AUC.

DISCUSSION

In this study a multimodality flow phantom was used to compare the AIFs derived from 3D-FLASH magnitude and phase signals, against the gold standard DCE-CT under similar conditions (including use of Gd-DTPA for CT investigation). Magnitude signal-derived AIF is sensitive to imaging orientation, flip angle, and in-flow effects, as demonstrated by prior authors. We show that implementation of position and velocity-matched T1 measurements can improve the magnitude signal-derived AIF measurement, yet equivalence to CT was noted only at peak Gd-DTPA concentrations to 2.5 mM. In comparison, phase-derived AIF showed equivalence to CT within 1 mM across the range of tested conditions, plus robustness to imaging orientation, flip angle, and in-flow effects. However, the phase AIF overshot the CT AIF for low concentrations.

Magnitude Signal-Derived AIF Measurements

Conversion of the magnitude signal to concentration using the standard FLASH signal equation leaves the AIF_{MAGN} measurement prone to a number of biases. Saturation of the nonlinear FLASH signal owing to T1 and T_2* properties of gadolinium is a known problem (29). In addition, the magnetic susceptibility

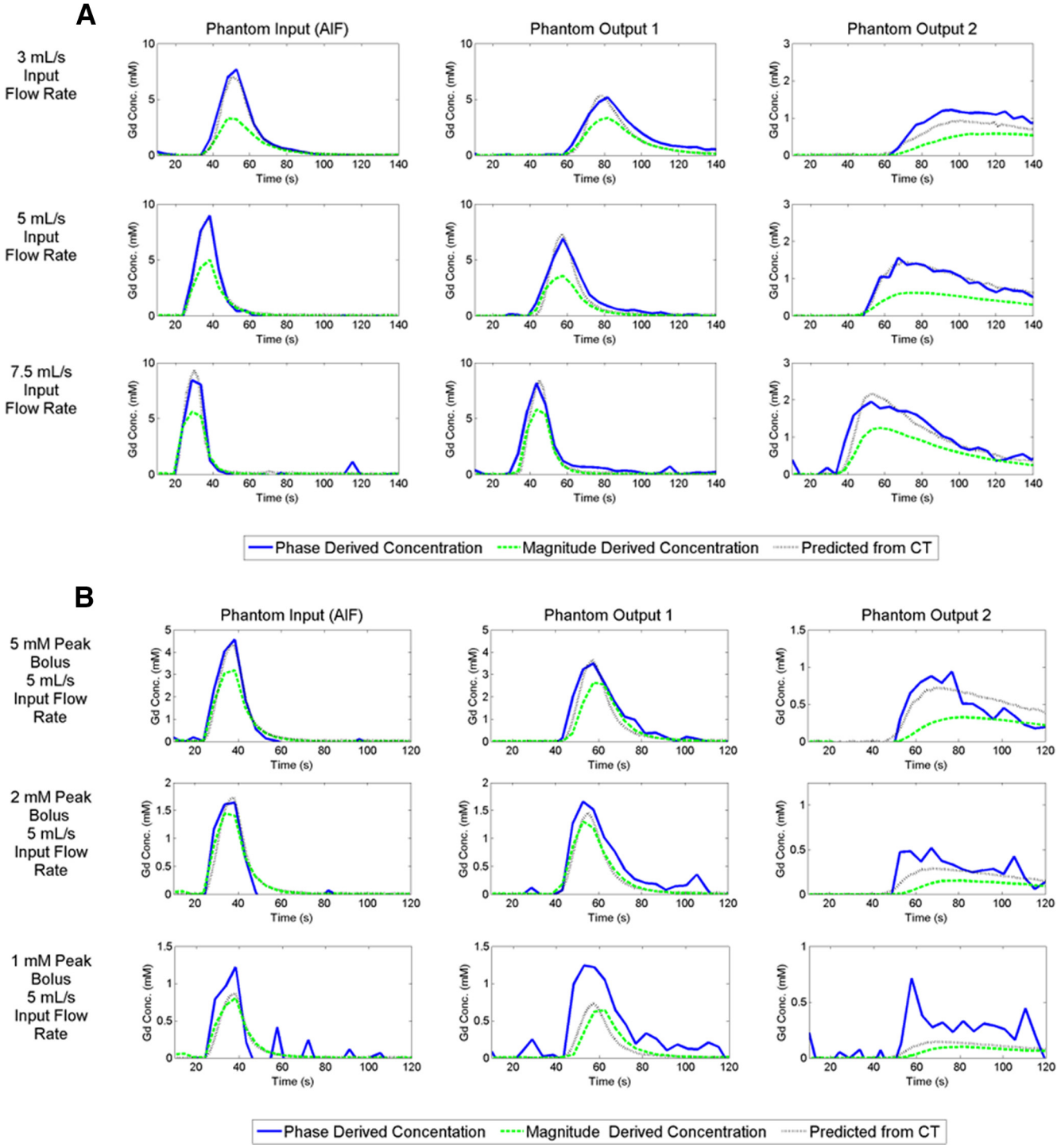

Figure 8. AIF_{PHA} compared to AIF_{MAGN} at a flip angle of 30° and AIF_{CT} for: (A) peak concentrations of 10 mM at increasing flow rates and for (B) 5 mL/s through-plane flow rate with increasing peak Gd-DTPA concentrations.

offset at peak bolus concentration may introduce a mis-registration artifact (18).

This research investigated RF and inflow biases to the 3D-FLASH magnitude signal, and it showed dramatic underestimation of AIF_{MAGN} metrics (28). RF and inflow biases were particularly severe for through-plane flow compared to in-plane flow, consistent with Garpenbring et al. (10). Inflow effects were partially compensated by incorporation of flow and position-matched VFA-T1 measurements into equation (1). The T1 correction is intuitive because the rate of inflow from outside of the imaging volume is captured as an acceleration of R_1 (26). However, even with this correction, our AIF_{MAGN} measurements were significantly different from AIF_{CT} except at peak Gd-DTPA concentrations <2.5 mM. Korporaal et al. also presented with a

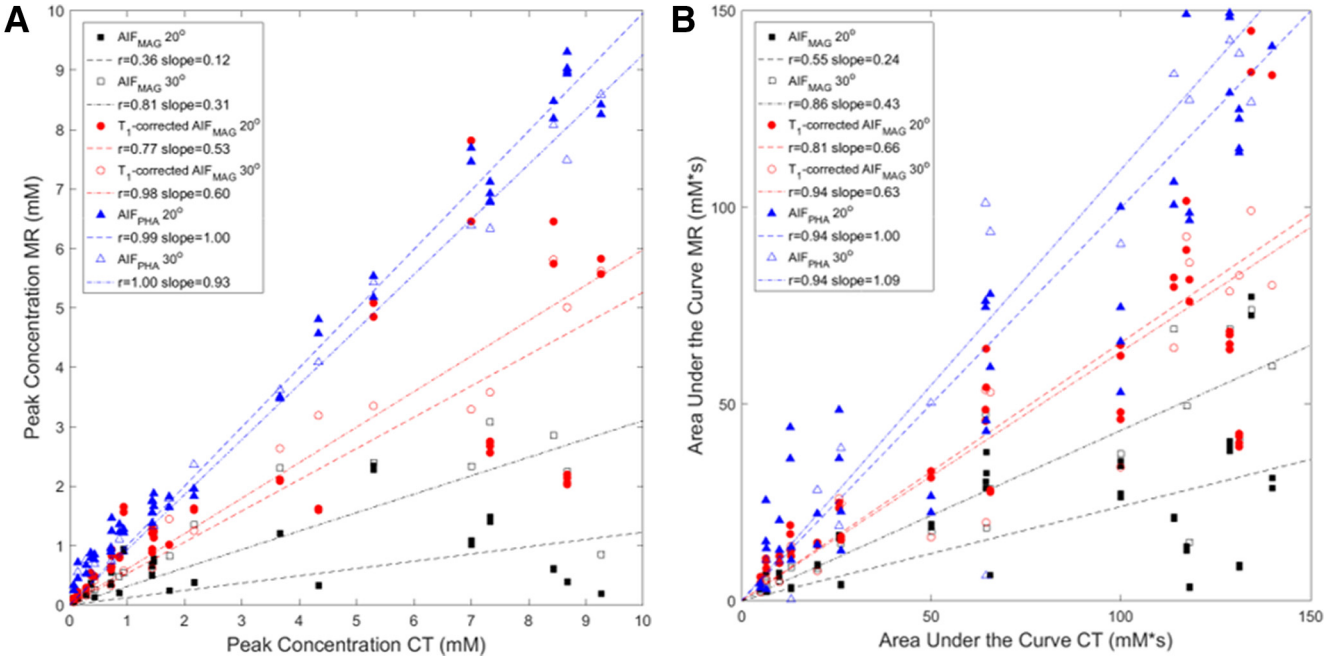

Figure 9. Pearson correlation results for AIF_{MAGN} and AIF_{PHA} compared to AIF_{CT}, for (A) peak concentration, and (B) AUC measurements within a central slice. The different shapes represent the 3 data types evaluated, pooled across velocities and concentrations for through-plane flow at flip angles of 20 (filled symbols, 16 runs, 48 measurements in input and output tubes) and 30° (open symbols, 7 runs, 21 measurements in input and output tubes).

considerably underestimated AIF_{MAGN} compared to AIF_{PHA} and AIF_{CT} targeting the femoral artery of patients with prostate cancer (17).

A key issue for the current multimodal phantom design is the need for a higher T1 relaxivity glycerol/water mixture to sustain CompuFlow pump performance. A peristaltic pump would convect water instead, at the cost of reproducibility in performance because of residual pulsatility, deviation from expected flow under high downstream pressure, and tube stretch over time. At the measured T1 relaxivity of 7.5 1/mM*s, the MR magnitude signal to Gd-DTPA concentration conversion saturates at lower concentrations than would be expected for Gd-DTPA within saline or plasma (T1 relaxivity, ~5.0 1/mM*s). This saturation is exacerbated at lower flip angles (eg, saturation of 10° flip angle data at ~2.5 mM in Figure 3C).

Dynamic measurement analysis at high Gd-DTPA concentrations can also be compromised by T_2* relaxation, because T_2* relaxation times of the 15% glycerol/water mixture appear to be well within an order of magnitude of the TE at concentrations above 5 mM. Our image processing assumed negligible T_2* relaxation, in part because experimental TE values are generally short relative to T2*, but it was also infeasible to measure T_2* at each Gd-DTPA concentration during the dynamic experiment. Schabel et al. published a nonlinear concentration-independent solution to the dynamic analysis problem, but logic and accurate knowledge of T_2* are necessary for selection of the correct concentration following saturation (28). Sufficient signal-to-noise must also exist for differentiation between concentrations, and the dynamic range of the signal across concentrations reduces with flip angle.

Another likely issue affecting the 3D-FLASH magnitude signal during dynamic experiments is its transient nature. At high flow rates, the magnetization may be exposed to an insufficient number of RF pulses to achieve steady-state condition, which is further compounded by spatially varying RF amplitudes. At low flow rates for through-plane flow, the magnetization may also be exposed to spatially varying RF amplitude along the shoulder region of the RF pulse slice profile. Consequently, some groups advocate AIF_{MAGN} measurement in ROI locations, where the steady-state condition is better satisfied (11, 21). Use of higher flip angles also improves AIF_{MAGN} robustness by accelerating the transition to steady state (25).

One may also expect better comparative performance at higher flip angles because of improved 3D-FLASH signal linearity with Gd-DTPA concentration, consistent with our results in Figure 2 and the published comparative measurements from Cron et al. (20). However, the improved signal linearity comes at a price of SNR and specific absorption ratio, factors which can prohibit implementation of high spatial resolution and high temporal resolution brain protocols with considerable coverage (eg, 1.5 × 1.5 × 3 mm spatial resolution, 6-second temporal resolution, 12 cm of through-plane coverage).

Phase-Signal-Derived AIF Measurements

The phase of the MR signal provides a mechanism for AIF quantification based on the magnetic susceptibility of Gd-DTPA. Our findings show that $AIFP_{HA}$ peak concentration measurements are equivalent within 1 mM to gold standard AIF_{CT} to a concentration of 10 mM, which covers the clinically relevant concentration range for AIF measurement (25). The AIF_{PHA} was

Table 2. 95% Limits of Agreement (LoA) for Peak Concentration and AUC Measurements Defined from Bland–Altman Difference Analysis Between MRI- and CT-derived AIF

Data Type	Data Range (mM)	Peak Concentration (mM)	AUC (mM*s)
AIF_{PHA}, FA 20°	0–10	0.1 ± 0.7	0.6 ± 37.0
AIF_{PHA}, FA 30°	0–10	−0.1 ± −0.9	3.6 ± 43.6
AIF_{PHA}, FA 20°	0–5	0.3 ± 0.4	3.4 ± 27.3
AIF_{PHA}, FA 30°	0–5	0.1 ± 0.4	2.6 ± 32.6
AIF_{PHA}, FA 20°	0–2	0.3 ± 0.4	5.9 ± 27.3
AIF_{PHA}, FA 30°	0–2	0.2 ± 0.4	−3.8 ± 20.3
Uncorrected AIF_{MAGN}, FA 20°	0–10	−2.8 ± 6.2	−52.5 ± 85.9
Uncorrected AIF_{MAGN}, FA 30°	0–10	−1.9 ± 4.9	−35.4 ± 64.7
Uncorrected AIF_{MAGN}, FA 20°	0–5	−0.9 ± 2.4	−15.5 ± 34.7
Uncorrected AIF_{MAGN}, FA 30°	0–5	−0.6 ± 1.6	−10.7 ± 24.1
Uncorrected AIF_{MAGN}, FA 20°	0–2	−0.4 ± 2.4	−6.8 ± 34.7
Uncorrected AIF_{MAGN}, FA 30°	0–2	−0.2 ± 0.5	−4.7 ± 8.2
T_1-corrected AIF_{MAGN}, FA 20°	0–10	−1.4 ± 4.3	−23.4 ± 58.4
T_1-corrected AIF_{MAGN}, FA 30°	0–10	−1.2 ± 2.8	−23.3 ± 44.6
T_1-corrected AIF_{MAGN}, FA 20°	0–5	−0.4 ± 1.7	−6.7 ± 23.9
T_1-corrected AIF_{MAGN}, FA 30°	0–5	−0.3 ± 0.8	−6.6 ± 19.6
T_1-corrected AIF_{MAGN}, FA 20°	0–2	−0.1 ± 1.7	−0.8 ± 23.9
T_1-corrected AIF_{MAGN}, FA 30°	0–2	−0.1 ± 0.2	0.6 ± 37.0

The table entries report the 95% LoA for each parameter as the average difference ± 1.96 standard deviation of the difference across variable concentrations and flow rates. The statistical analyses are repeated across 3 ranges of input tube concentrations.

also spatially robust in both in-plane and through-plane flow orientations, and to flow velocity and flip angle. This improved and more robust performance is consistent with the results from other groups. Korporaal et al. compared AIF_{MAGN}, AIF_{PHA}, and AIF_{CT}, targeting the femoral artery in patients with prostate cancer (17). Cron et al. favorably compared AIF_{PHA} to AIF_{MAGN} in the femoral artery, but without measurement of vascular T1 or AIF_{CT} validation (20). The same group has also applied phase imaging to calculate the venous input function in the superior sagittal sinus (30).

A limiting factor for the phase AIF measurement is precision at low Gd-DTPA concentrations, because the phase shift is small and imprecisely measured. Gd-DPTA increases the SNR in T1-weighted magnitude images, and phase noise varies inversely with the SNR in magnitude images (31). For this reason, the analysis of data presented in experiment 6 considers only the middle 60% of the imaging slices.

A number of factors can further impact the use of AIF_{PHA} in the clinical setting. First, 3D-FLASH phase reconstruction may not be accessible on clinical MRI systems in the absence of a research license or key. Second, vessel selection for AIF_{PHA} measurements may be limited to large vessels (eg, femoral artery, sagittal sinus, internal carotid artery) owing to the need for sufficient vessel diameter to reduce partial volume effects, and the increasing complexity of modeling of magnetic susceptibility effects when vessel orientation and shape diverges from that of a cylinder aligned in parallel with B_0 (22). Finally, phase wrap during bolus passage requires automated postprocessing, or manual correction by modulo 360° shifts in the phase image (32, 33).

A need for background phase correction is a complication of the AIF_{PHA} measurement. Our flow phantom experiments used a single control tube satisfactorily; yet, the phase signal calibration was stabilized against off-resonance effects when the Gd-DTPA-doped sample tube was surrounded with a hexagonal array of control tubes. Residual static field inhomogeneity will also exist across the brain in vivo, and within the sagittal sinus itself (34), which may complicate selection of an ROI for background phase correction in vivo. Our own experiences (unpublished) also suggest that the sagittal sinus AIF_{PHA} measurement is improved at lower flip angles for reasons that require further investigation and yet may suggest a combination of off-resonance and RF heating effects. However, any RF heating effects should be apparent in the brain parenchyma but not in the sinus owing to convection. Alternatively, field camera technology can capture the temporal and spatial history of resonance frequency changes during phase-sensitive acquisitions (35, 36). Also, the fat resonance provides a temperature-insensitive phase reference that should enable tracking of instrumentation-related resonance frequency changes (37).

Clinical Relevance

The value of individualized patient AIF acquisition is not yet fully understood. Port et al. showed that in 23% of patients, the individual's AIF differs from the population average by >50%

(38), and it is possible that the use of population-average AIFs may limit our ability to meaningfully interpret DCE-MRI findings, and this variability may contribute to the high inconsistency in permeability measures reported in prior DCE-MRI studies. Ashton et al. showed a 70% reduction of visit-to-visit coefficient of variation in permeability parameters using individual compared with population AIFs (39). However, several publications have shown equivalence in pharmacokinetic output parameters when DCE-MRI data are analyzed using population average or individualized measurements (13, 40). These findings may reflect on-going challenges to measure individual AIF accurately. This study shows that AIF_{PHA} could provide a feasible supplemental method for individual AIF acquisition with greater accuracy and robustness such that this approach may improve the consistency in the results of future DCE-MRI studies.

The technical requirements for a dynamic MRI phantom for quality assurance testing are currently not well understood. However, recognizing that site and system factors that compromise shim performance and temperature regulation of hardware components may compromise phase-based AIF evaluation within clinical trials, the roles of a flow phantom may include to measure and consider differences across sites and scanners when interpreting data, as well as to monitor system performance. It is important to note that factors affecting phase may not be captured by standardized QA protocols that focus on magnitude signal metrics. The phantom could also be modified to account for partial voluming, and vessels of smaller calibers.

In summary, we use a controlled multimodal flow phantom that is validated against AIF_{CT} to show that AIF_{PHA} tracks peak Gd-DTPA concentration within 1 mM, and AUC within 44 mM*s, over a range of tested conditions. The robustness of the AIF_{PHA} measurements was also apparent across the imaged volume. In comparison, AIF_{MAGN} measurements were highly sensitive to imaging plane orientation, flip angle selection, and flow velocity, and equivalent performance to AIF_{CT} was shown at only Gd-DTPA concentrations <2 mM. Improving the accuracy of the AIF should reduce variability in pharmacokinetic output parameters, and thereby, it should increase the potential for meaningful interpretation of the changes in vascular permeability using DCE-MRI.

ACKNOWLEDGMENTS

This work was partially supported by Discovery Grant 386277 from the National Science and Research Council of Canada (NSERC), the Brain Tumor Foundation of Canada Pilot Grant, and the Princess Margaret Cancer Foundation—Department of Radiation Oncology Academic Enrichment Fund.

Equal Contribution: Coolens C. and Chung C. contributed equally to this paper.

Disclosures: No disclosures to report.

Conflict of Interest: The authors have no conflict of interest to declare.

REFERENCES

1. O'Connor JP, Jackson A, Parker GJ, Roberts C, Jayson GC. Dynamic contrast-enhanced MRI in clinical trials of antivascular therapies. Nat Rev Clin Oncol. 2012;9:167–177.
2. Leach M, Morgan B, Tofts P, Buckley DL, Huang W, Horsfield MA, Chenevert TL, Collins DJ, Jackson A, Lomas D, Whitcher B, Clarke L, Plummer R, Judson I, Jones R, Alonzi R, Brunner T, Koh DM, Murphy P, Waterton JC, Parker G, Graves MJ, Scheenen TW, Redpath TW, Orton M, Karczmar G, Huisman H, Barentsz J, Padhani A; Experimental Cancer Medicine Centres Imaging Network Steering Committee. Imaging vascular function for early stage clinical trials using dynamic contrast-enhanced magnetic resonance imaging. Eur Radiol. 2012;22:1451–1464.
3. O'Connor JPB, Jackson A, Parker GJM, Jayson GC. DCE-MRI biomarkers in the clinical evaluation of antiangiogenic and vascular disrupting agents. Brit J Cancer. 2007;96:189–195.
4. Heye T, Davenport MS, Horvath JJ, Feuerlein S, Breault SR, Bashir MR, Merkle EM, Boll DT. Reproducibility of dynamic contrast-enhanced MR imaging. Part I. Perfusion characteristics in the female pelvis by using multiple computer-aided diagnosis perfusion analysis solutions. Radiology. 2013;266:801–811.
5. Heye T, Merkle EM, Reiner CS, Davenport MS, Horvath JJ, Feuerlein S, Breault SR, Gall P, Bashir MR, Dale BM, Kiraly AP, Boll DT. Reproducibility of dynamic contrast-enhanced MR imaging. Part II. Comparison of intra- and interobserver variability with manual region of interest placement versus semiautomatic lesion segmentation and histogram analysis. Radiology. 2013;266:812–821.
6. Tofts PS. Modeling tracer kinetics in dynamic Gd-DTPA MR imaging. J Magn Reson Imaging. 1997;7:91–101.
7. Yang X, Knopp MV. Quantifying tumor vascular heterogeneity with dynamic contrast-enhanced magnetic resonance imaging: a review. J Biomed Biotechnol. 2011;2011:1–12.
8. Yang X, Liang J, Heverhagen JT, Jia G, Schmalbrock P, Sammet S, Koch R, Knopp MV. Improving the pharmacokinetic parameter measurement in dynamic contrast-enhanced MRI by use of the arterial input function: Theory and clinical application. Magn Reson Med. 2008;59:1448–1456.
9. Peeters F, Annet L, Hermoye L, van Beers BE. Inflow correction of hepatic perfusion measurements using T1-weighted, fast gradient-echo, contrast-enhanced MRI. Magn Reson Med. 2004;51:710–717.
10. Garpebring A, Wirestam R, Östlund N, Karlsson M. Effects of inflow and radiofrequency spoiling on the arterial input function in dynamic contrast-enhanced MRI: A combined phantom and simulation study. Magn Reson Med. 2011;65:1670–1679.
11. Roberts C, Little R, Watson Y, Zhao S, Buckley DL, Parker GJ. The effect of blood inflow and B1-field inhomogeneity on measurement of the arterial input function in axial 3D spoiled gradient echo dynamic contrast-enhanced MRI. Magn Reson Med. 2011;65:108–119.
12. van Osch MJP, Vonken EPA, Viergever MA, van der Grond J, Bakker CJ. Measuring the arterial input function with gradient echo sequences. Magn Reson Med. 2003;49:1067–1076.
13. Meng R, Chang SD, Jones EC, Goldenberg SL, Kozlowski P. Comparison between population average and experimentally measured arterial input function in predicting biopsy results in prostate cancer. Acad Radiol. 2010;17:520–525.
14. Li X, Welch EB, Arlinghaus LR, Chakravarthy AB, Xu L, Farley J, Loveless ME, Mayer IA, Kelley MC, Meszoely IM, Means-Powell JA, Abramson VG, Grau AM, Gore JC, Yankeelov TE. A novel AIF tracking method and comparison of DCE-MRI parameters using individual and population-based AIFs in human breast cancer. Phys Med Biol. 2011;56:5753–5769.
15. Yankeelov TE, Cron GO, Addison CL, Wallace JC, Wilkins RC, Pappas BA, Santyr GE, Gore JC. Comparison of a reference region model with direct measurement of an AIF in the analysis of DCE-MRI data. Magn Reson Med. 2007;57:353–361.
16. Lavini C, Verhoeff JJC. Reproducibility of the gadolinium concentration measurements and of the fitting parameters of the vascular input function in the superior sagittal sinus in a patient population. Magn Reson Imaging. 2010;28:1420–1430.
17. Korporaal JG, van den Berg CA, van Osch MJ, Groenendaal G, van Vulpen M, van der Heide UA. Phase-based arterial input function measurements in the femoral arteries for quantification of dynamic contrast-enhanced (DCE) MRI and comparison with DCE-CT. Magn Reson Med. 2011;66:1267–1274.
18. Akbudak E, Norberg RE, Conturo TE. Contrast-agent phase effects: An experimental system for analysis of susceptibility, concentration, and bolus input function kinetics. Magn Reson Med. 1997;38:990–1002.
19. Garpenbring A, Wirestam R, Yu J, Asklund T, Karlsson M. Phase-based arterial input functions in humans applied to dynamic contrast-enhanced MRI: potential usefulness and limitations. Magn Reson Mater Phys. 2011;24:233–245.

20. Cron GO, Foottit C, Yankeelov TE, Avruch LI, Schweitzer MR, Cameron I. Arterial input functions determined from MR signal magnitude and phase for quantitative dynamic contrast-enhanced MRI in the human pelvis. Magn Reson Med. 2011; 66:498–504.
21. Driscoll B, Keller H, Jaffray DA, Coolens C. Development of a dynamic quality assurance testing protocol for multisite clinical trial DCE-CT accreditation. Med Phys. 2013; 40:081906.
22. Schenck JF. The role of magnetic susceptibility in magnetic resonance imaging: MRI magnetic compatibility of the first and second kinds. Med Phys. 1996;23:815–850.
23. Cheng H-LM, Wright GA. Rapid high-resolution T1 mapping by variable flip angles: accurate and precise measurements in the presence of radiofrequency field inhomogeneity. Magn Reson Med. 2006;55:566–574.
24. Takeuchi S, Karino T. Flow patterns and distributions of fluid velocity and wall shear stress in the human internal carotid and middle cerebral arteries. World Neurosurg. 2010;73:174–185.
25. De Naeyer D, Verhulst J, Ceelen W, Segers P, De Deene Y, Verdonck P. Flip angle optimization for dynamic contrast-enhanced MRI-studies with spoiled gradient echo pulse sequences. Phys Med Biol. 2011;56:5373–5395.
26. Bauer WR, Hiller KH, Roder F, Rommel E, Ertl G, Haase A. Magnetization exchange in capillaries by microcirculation affects diffusion-controlled spin-relaxation: a model which describes the effect of perfusion on relaxation enhancement by intravascular contrast agents. Magn Reson Med. 1996;35:43–55.
27. Brookes JA, Redpath TW, Gilbert FJ, Murray AD, Staff RT. Accuracy of T1 measurement in dynamic contrast-enhanced breast MRI using two- and three-dimensional variable flip angle fast low-angle shot. J Magn Reson Imaging. 1999; 9:163–171.
28. Schabel MC, Parker DL. Uncertainty and bias in contrast concentration measurements using spoiled gradient echo pulse sequences. Phys Med Biol. 2008;53: 2345–2373.
29. de Bazelaire C, Rofsky N, Duhamel G, Zhang J, Michaelson MD, George D, Alsop DC. Combined T2* and T1 measurements for improved perfusion and permeability studies in high field using dynamic contrast enhancement. Eur Radiol. 2006;16:2083–2091.
30. Foottit C, Cron GO, Hogan MJ, Nguyen TB, Cameron I. Determination of the venous output function from MR signal phase: feasibility for quantitative DCE-MRI in human brain. Magn Reson Med. 2010;63:772–781.
31. Conturo TE, Smith GD. Signal-to-noise in phase angle reconstruction: dynamic range extension using phase reference offsets. Magn Reson Med. 1990;15:420–437.
32. Liu J, Drangova M. Intervention-based multidimensional phase unwrapping using recursive orthogonal referring. Magn Reson Med. 2012;68:1303–1316.
33. Chavez S, Xiang Q-S, An L. Understanding phase maps in MRI: a new cutline phase unwrapping method. IEEE T Med Imaging. 2002;21:966–977.
34. Jain V, Langham MC, Wehrli FW. MRI estimation of global brain oxygen consumption rate; J Cereb Blood Flow Metab. 2010;30:1598–1607.
35. De Zanche N, Barmet C, Nordmeyer-Massner JA, Pruessmann KP. NMR probes for measuring magnetic fields and field dynamics in MR systems. Magn Reson Med. 2008;60:176–186.
36. Boer VO, van de Bank BL, van Vliet G, Luijten PR, Klomp DW. Direct B0 field monitoring and real-time B0 field updating in the human breast at 7 Tesla. Magn Reson Med. 2012;67:586–591.
37. Hofstetter LW, Yeo DT, Dixon WT, Kempf JG, Davis CE, Foo TK. Fat-referenced MR thermometry in the breast and prostate using IDEAL. J Magn Reson Imaging. 2012;36:722–732.
38. Port RE, Knopp MV, Brix G. Dynamic contrast-enhanced MRI using Gd-DTPA: interindividual variability of the arterial input function and consequences for the assessment of kinetics in tumors. Magn Reson Med. 2001;45:1030–1038.
39. Ashton E, Raunig D, Ng C, Kelcz F, McShane T, Evelhoch J. Scan-rescan variability in perfusion assessment of tumors in MRI using both model and data-derived arterial input functions. J Magn Reson Imaging. 2008;28:791–796.
40. Hormuth DA 2nd, Skinner JT, Does MD, Yankeelov TE. A comparison of individual and population-derived vascular input functions for quantitative DCE-MRI in rats. Magn Reson Imaging 2014;32:397–401.